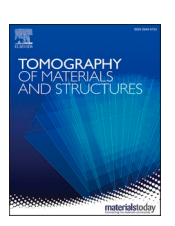
ELSEVIER

Contents lists available at ScienceDirect

Tomography of Materials and Structures

journal homepage: www.journals.elsevier.com/tomography-of-materials-and-structures





Dual-energy computed tomography for improved contrast on a polyphase graphitic ore

Leonard T. Krebbers ^{a,*}, Natalia Grozmani ^b, Bernd G. Lottermoser ^a, Robert H. Schmitt ^b

- a RWTH Aachen University, Institute of Mineral Resources Engineering, Wüllnerstraße 2, Aachen 52062, Germany
- b RWTH Aachen University, Laboratory for Machine Tools and Production Engineering, Chair of Production Metrology and Quality Management, Campus Boulevard 27, Aachen 52062, Germany

ARTICLE INFO

Keywords: Dual-energy computed tomography Ore geology 3D imaging Natural graphite Graphite extraction

ABSTRACT

Proper ore characterisation is essential for understanding ore deposits and developing efficient mineral processing flow sheets. Conventional mineralogical and chemical techniques are usually used to study ores, but they can be destructive and, in some cases, provide only 2D information. Computed tomography (CT) is an emerging technology in the raw materials sector enabling the non-destructive 3D analysis of the ore mineralogy and microstructure. However, single-energy CT (SECT) has some limitations concerning the accurate imaging and differentiation of polyphase geomaterials comprising a broad range of attenuation properties. By contrast, dual-energy CT (DECT) uses two different X-ray energies to acquire data, which can be used to distinguish between materials with similar attenuation properties. This study explored the application of DECT for the analysis of a polyphase graphitic ore. A sequential fusion approach was utilized to combine data obtained from different X-ray energy scans at high spatial resolution, and varying weighting factors were applied to determine the optimal contribution of each energy level and spectrum. Both, SECT and DECT datasets were quantitatively evaluated based on the contrast-to-noise-ratio (CNR) and Q factor. The findings demonstrate that DECT significantly improves image contrast compared to SECT while further increases image sharpness. As a result, DECT may enable more accurate segmentation and, therefore, more accurate quantitative 3D analysis of graphite ores.

1. Introduction

An accurate assessment of ore deposits and the development of efficient extraction of ore minerals rely on a solid understanding of their mineralogy as well as their physical and chemical properties. To obtain this information, various analytical methods are employed, such as optical microscopy (OM), scanning electron microscopy equipped with an energy or wavelength dispersive X-ray analyser (SEM/E-WDX), electron microprobe analyser (EMPA), secondary ion mass spectrometry (SIMS), laser ablation inductively coupled plasma mass spectrometry (LA-ICP-MS), and X-ray diffraction (XRD) [1-4]. In recent decades, computed tomography (CT) has proven its added value in studying the mineralogical aspects of geological materials, with an increasing number of studies recognizing its advantages for investigating rocks and ores [5-13]. Unlike conventional methods, CT offers quantitative and non-destructive 3D analysis with minimal sample preparation, eliminating the stereological bias [14–16]. This includes the ability to provide direct and more representative information on the shape, orientation,

and size of phases without the need for time-consuming sectioning.

The CT principle is based on the X-ray attenuation behaviour of the phases comprising the sample, which is displayed by the contrast produced in the resulting greyscale image. The X-ray attenuation varies as a function of the material density, the average atomic number, and the thickness of the scanned object, as well as the X-ray energy applied [17, 18]. This difference in X-ray linear attenuation provides a contrast which can be used for mineral differentiation.

The effective utilization of CT depends on the X-ray beam's capability to penetrate the sample, enabling the visualization of internal geometry [18,19]. However, CT struggles to accentuate or distinguish between features that exhibit similar densities and effective atomic numbers. In this regard, ores often comprise complex polyphase geomaterials with a wide range of X-ray attenuation properties owing to their constituents' differences and/or similarities in density, atomic number, and particle sizes. This can make it challenging to acquire high-quality CT data of these materials, as it can lead to scanning artifacts and mixed attenuation coefficients that result in a partial overlap of

E-mail address: krebbers@mre.rwth-aachen.de (L.T. Krebbers).

^{*} Corresponding author.

grey values in the reconstructed CT greyscale image stack that hamper the interpretation and processing of CT data [20–22].

To obtain high-quality CT data, the proper X-ray energy must be selected, to optimise data quality, which is not always straightforward [23]. Higher X-ray energy is required to penetrate high-density materials or thicker sections, but it may cause a loss of contrast and unresolvable features. Conversely, using lower X-ray energy to obtain good quality imaging of light materials may not penetrate denser materials, resulting in loss of information [22,24]. Thus, the choice of the advantageous beam intensity must be a trade-off between high and low-absorbing materials within the specimen to be examined.

Current and past research focused on the acquisition of high CT data primarily through the development of scanning protocols for the optimal scanning parameters to extract mineralogical and textural information in ore samples [8,25,26] and the development of an attenuation coefficient data bank in order to predict phase discrimination in ores [27, 28]. Another method that may contribute to the generation of high-quality CT scans of complex ores is dual-energy computed tomography (DECT). DECT has been widely established in medical imaging, sorting, and security applications [29-32]. Notably, in the medical field, DECT has become a routine method for detecting anatomic structures and conducting contrast-enhanced studies to improve image quality [33-37]. In the context of analysing geomaterials, DECT has primarily been used for material decomposition [38-41]. By utilizing two different X-ray energies, DECT enables the tracking of attenuation changes according to the X-ray spectra. This information can be harnessed to identify minerals in the samples and retrieve their density and effective atomic number (Zeff) information. However, studies applying DECT to a polyphase ore and quantifying the improvement in image quality are sparse.

This study aims to investigate the potential of high-resolution DECT for enhancing image contrast in a heterogeneous polyphase graphitic ore. The study utilizes a sequential fusion approach to combine data obtained from different X-ray energy scans at high spatial resolution. Various X-ray energy spectra are combined with varying weighting factors to determine the favourable contribution of each energy level and spectrum, thereby aiming to provide the best possible attenuation of each phase. The findings of this study provide valuable insights into the establishment of DECT data and demonstrate the effectiveness of DECT in improving image quality in the context of complex geomaterials.

2. Materials and methods

2.1. Conventional analysis

A polymineralic flake graphite ore was provided by Westwater Resources, Inc. (Centennial, Colorado, USA). The specimen originates from the Bama Graphite Mine (Chilton Co., Alabama, USA), and consists of variable amounts of graphite as well as gangue phases (i.e., quartz, clay, muscovite, hydrated iron(III) oxide-hydroxides (HFO)). Mineralogicalpetrographic investigations, including XRD, OM and SEM-EDS, were carried out prior to the CT measurements. XRD was used to determine the bulk mineralogy of the graphite ore sample. These steps are necessary to correctly interpret the CT data. For XRD analysis, a 2.5 g sample was ground in 100 % ethanol for 5 min using a McCrone micronizing mill with synthetic agate pellets. After air-drying, the micronized aliquots underwent qualitative phase identification using the JADE (Rigaku, Tokyo, Japan) and EVA (Bruker, Billerica, MA, USA) software packages on a Rigaku Ultima IV powder X-ray diffractometer (Department of Earth and Atmospheric Sciences, University of Alberta, Edmonton, Canada). Mineral phases were identified by referencing the ICDD PDF4 + database. For petrographic analysis, a thin section, and a cylindrical-shaped polished block (12 mm in diameter, 5 mm in height) were prepared by MK Factory (Stahnsdorf, Germany). Both, the thin section, and the polished block were examined using a LEICA DM 2700 P polarisation microscope (Institute of Mineral Resources Engineering,

RWTH Aachen University, Germany), and microphotographs were taken using a LEICA FLEXCAM C1 camera and the LEICA LAS software. The polished block was subject to SEM-EDS analysis to further investigate the mineralogy and microstructure of the graphite ore specimen, using a FEI 650 F scanning electron microscope equipped with two Bruker XFlash 5030 detectors (Institute of Mineralogy and Economic Geology, RWTH Aachen University, Germany) at 15 kV and 10 nA.

2.2. Computed tomography

A CT-ALPHA micro-CT system (ProCon X-ray GmbH, Sarstedt, Germany) was used, which is equipped with a five-axes-manipulation system between an XWT-240-TCHE plus X-ray tube with a maximum voltage of 240 kV and an XRD 1611 AP3 detector system with 4096 \times 4096 pixels (100 mm²) (Institute of Mineral Resources Engineering, RWTH Aachen University, Germany). The CT investigation was executed on the cylindrically shaped, polished block mentioned before. The specimen was placed between the X-ray source and the detector on the rotating table. The resulting CT measurement is the collection of 2D sample projections (radiographs), taken as the sample rotates 360° around the vertical axis between the X-ray tube and the detector. The detector collects the intensity of transmitted X-ray photons of each projection and thus provides X-ray attenuation information. Based on this information, an X-ray attenuation coefficient is calculated for each pixel of the sample projection. This coefficient is displayed as a distinct grey-scale value in the projection image [42]. The acquired radiographs are subsequently processed using a reconstruction algorithm to produce a 3D volume represented by a cubic matrix of grayscale voxels (3D pixels).

2.3. Fundamentals of dual-energy computed tomography

Selecting appropriate acquisition parameters (e.g., voltage, current, integration time) for a polyphase sample like the one used in this study (i.e., a graphitic ore), comprising both, high and low X-ray attenuating minerals, is a crucial step that has to ensure that the radiation will also pass through the thickest and highest absorbing phase of the sample. Insufficient intensity can compromise the quality of the reconstructed image, complicating subsequent image processing. In theory, lower energy will increase the grayscale contrast of the reconstructed volume, while measuring with higher energy decreases any imaging artifacts but at the same time may reduce the contrast between low-absorbing phases with similar densities and different compositions.

The main principle of dual-energy computed tomography (DECT) is to combine attenuation information from two conventional or single-energy CT (SECT) scans performed at different X-ray energy levels to obtain a high-quality, single dataset. SECT scans can be fused before, after, or simultaneously with CT volume reconstruction. The CT scans fusion in this work was performed before the reconstruction and is based on a weighted linear combination of the respective low and high-voltage SECT projection stacks:

$$f_{FI,\alpha} = \alpha \bullet f_{HV} + ((1 - \alpha) \bullet f_{LV}) \tag{1}$$

where $f_{PI,\alpha}$ represents the fused projection image obtained through a weighted linear combination of the respective high-voltage (f_{HV}) and low-voltage projection (f_{LV}). The weighting factor, α , is chosen from the range of [0,1].

2.4. Scan protocol and procedures

The cylindrical-shaped polished block was sequentially measured using five different voltage settings with 60 kV, and 80 kV reflecting the low voltage range (LV scans) as well as $170 \, \text{kV}$, $180 \, \text{kV}$ and $190 \, \text{kV}$ comprising the high voltage range (HV scans). It is worth noting that maintaining an appropriate distance between the energy of the X-ray

spectra of the two measurements is essential for obtaining appropriate DECT data [43]. Since the desired resolution was at the lower micron-scale, the block was positioned close to the X-ray source (SOD=24.5 mm). The focal spot size was set to microfocus beam mode to further increase spatial resolution. The beam current was adjusted accordingly for each scan to operate with 8 W, and the number of projections and averaging were kept constant. The exposure time was set to 1.6 s for all LV scans. To avoid saturating the detector, the exposure time in the HV range had to be adjusted to 0.8 s. The CT set-up parameters are summarized in Table 1.

A Python script was used to generate the corresponding DECT raw data. Here, the weighting factors α were set to 0.3, 0.5, and 0.7 (Eq.1). A weight factor, of 0.3 for example results in 30 % of the high voltage projection, and 70 % of the low voltage projection image. All raw data collected were reconstructed using Volume Graphics VGStudio Max 3.5.0 [44]. Subsequently, 18 fused DECT datasets were generated, comprising six $HV \times LV$ combinations combined with three different weighting factors each.

2.5. Quality factors and statistical analysis

Grey value information for all reconstructed SECT and fused DECT datasets were obtained by placing regions of interest (ROI) in the following material areas (MA) (Fig. 1):

- Graphite attached to combined quartz and clay, hereafter referred to as MA1
- Graphite in the vicinity of a void/crack (air), hereafter referred to as MA2
- Muscovite associated with HFO, hereafter referred to as MA3
- Muscovite associated with quartz and clay, hereafter referred to as MA4.

The definition of the MAs was primarily based on the ore mineralogy's representativeness, target minerals focus, and grayscale intensity profiles. The material areas encompass five out of the seven identified phases and structures, with hematite and HFO excluded due to high mean grey value differences, facilitating straightforward segmentation. Every dataset contained 80 ROIs (10 ROIs for each phase and structure, or 20 ROIs per MA, respectively). After each ROI was created on the first analysed dataset, it was copied to the subsequent datasets to ensure they were identical in size, shape, and location. This resulted in 1840 ROIs considering all 23 datasets (five SECT acquisitions and 18 DECT datasets). Each individual ROI spanned multiple slices, with the specific three-dimensional extension determined by the attributes of the respective phases. Furthermore, care was taken to ensure that, to the greatest extent possible, each ROI exclusively contained a single material.

To simplify data extraction, two ROIs were placed adjacent to each other in each material area considered. This enabled the direct measurement of mean attenuation and standard deviation using the grey value analysis tool in VGStudio Max software, saving time, and

Table 1Set-up parameters for the acquisition of low-voltage (LV) and high-voltage (HV) CT-scans.

Energy range	LV		HV		
Voltage [kV]	60	80	170	180	190
Power [W]	8		8		
Binning [#x#]	2×2		2×2		
Exposure time [s]	1.6		0.8		
Number of projections [#]	1600		1600		
Resolution [μm x μm x μm]	6.8		6.8		
Prefilter [-]	none		Al 0.4		
Part orientation [°,°]	0		0		
Averaging [#]	14		14		

streamlining the analysis process. Consequently, this approach allowed the generation of a dense amount of attenuation information.

To quantitatively evaluate and compare the quality of each dataset, the contrast-to-noise ratio (CNR) was used to measure image quality in CT data. The CNR quantifies the ability to distinguish features in the scanned sample [45]. A higher CNR indicates higher grey value contrast and thus a better phase discrimination. Eq. 2 shows the calculation of the CNR, which measures the contrast as the difference between the mean grey values of the material and the background (μ_m and μ_b) divided by the background noise (σ_b):

$$CNR = \frac{Contrast}{Noise} = \frac{|\mu_m - \mu_b|}{\sigma_b}$$
 (2)

Here, graphite and muscovite were the targeted minerals of the four material areas as listed above, and quartz combined with clay, HFO and void/air are background materials. However, in some other applications, both materials in the pair are equally relevant. To avoid the possible discussion of the background definition, the Q factors [24,46,47], which describe the materials separation degree, were additionally analysed:

$$Q = \frac{|\mu_{m1} - \mu_{m2}|}{\sqrt{\sigma_{m1}^2 + \sigma_{m2}^2}} \tag{3}$$

The results below focus on the CNR-based analysis. However, Qfactor-based analysis delivers the same trend (see Appendix). In both cases, the quality factors were calculated for each ROI of each material area and dataset (local quality factors). The local CNR/Q-factors are the quality factor values for a single ROI pair in the same material area (Fig. 1). The mean values and the standard deviations were calculated based on ten local quality factors of the same material area. The global CNR/Q-factor was calculated once per material area and parameter combination, so it has no standard deviation. The global mean and standard deviation for each constituent in an MA were calculated using the grey values for each ROI. Therefore, the global CNR/Q-factors show the trends but cannot verify the significance of the absolute differences. Thus, local CNR/Q-factors, their means and standard deviations were used to quantify the results. To prove the significance of the differences in image quality and material attenuation among the various SECT and DECT measurements, a statistical analysis was performed. The multiple comparisons t-Test or paired t-tests with unequal variance, also known as the Fisher LSD test, was employed to compare the quality characteristics between the SECT and DECT datasets with different weighting factors. The Fisher LSD test starts from the hypothesis that the pair of given variances is similar and allocates them to two significantly distinguishable groups, if the probability of their similarity is less than a significance level. The significance level was set at 5 %. Each parameter combination was statistically analysed to define the significance of the mean value differences since calculated standard deviations were related to the mean values, not the global ones. Based on the test results, several significance groups were identified, and they are marked through letters from A to J (Group A reflects the highest CNR and Q factor values, and Group J (CNR) and Group G (Q factor) reflect the lowest). Parameter combinations in one significance group have no significant differences. Each parameter combination has been compared to all other combinations of the same ROIs pairwise. Therefore, the parameter combination could belong to more than one group.

3. Results

3.1. Pre CT analysis

The sample comprises a heavily altered graphitic ore with a quartz dominant matrix together with muscovite, clay, HFO, and hematite (Fig. 2). Graphite occurs as euhedral to subhedral flakes ranging from large (up to $1000~\mu m$ in length), usually subparallel elongated clusters, to small, disseminated flakes ($100-200~\mu m$ in length), which are

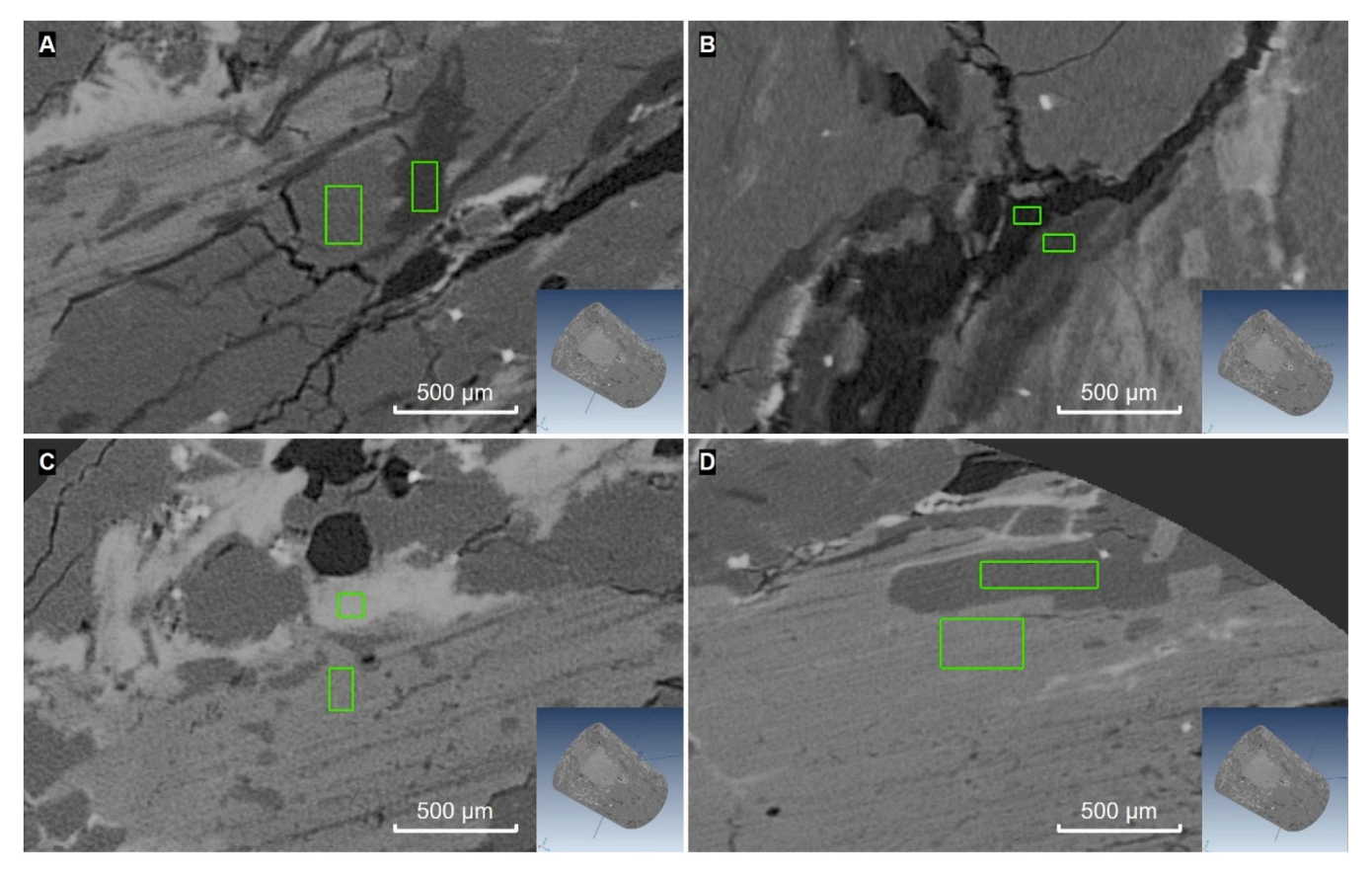


Fig. 1. ROI pairs of the different material areas (MAs) evaluated: a) graphite associated with quartz combined clay (MA1), b) graphite in the vicinity of a void or crack (MA2), c) muscovite associated with HFO (MA3) and d) muscovite associated with quartz combined clay (MA4). An individual ROI consists of multiple slices and relies on the 3D shape of the respective constituent.

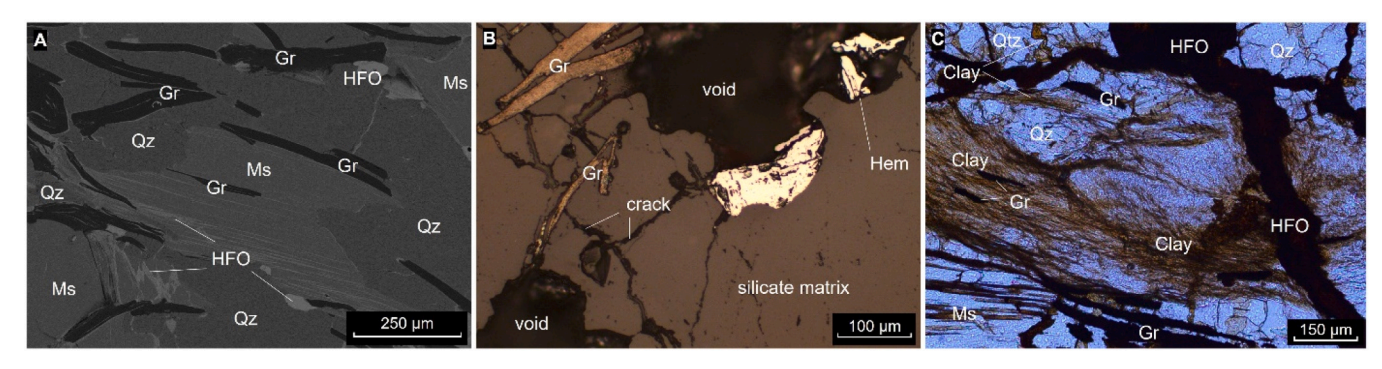


Fig. 2. SEM image (A), reflected light microscopy (B), and plane polarized light microscopy microphotograph (C) of different areas of the graphite ore sample. (A) Disseminated and subparallel orientated graphite flakes embedded in a silicate matrix of muscovite and quartz. HFO are present along cleavage planes of muscovite, pseudomorph after hematite (subhedral crystals) and occurs along grain boundaries and in veins. (B) Photomicrograph showing two voids and two anhedral hematite grains. Graphite flakes are present. A network of cracks occurs in the gangue matrix. (C) Brown coloured microcrystalline clay is present throughout the specimen area. Note the thick vein fill of HFO. Abbreviations: Graphite, Hem = hematite, HFO = hydrated iron(III) oxide-hydroxides, Ms = muscovite, Qz = quartz.

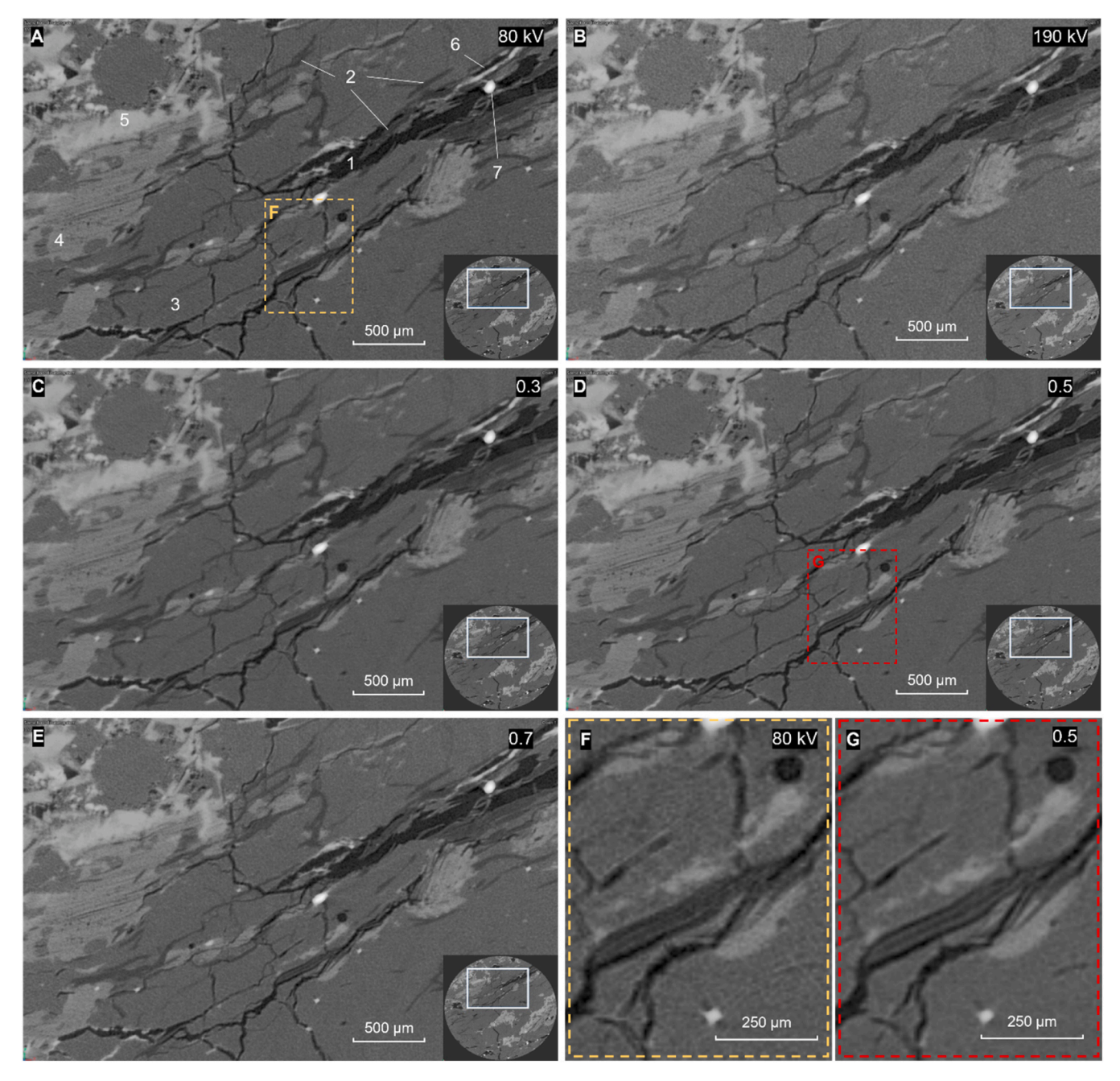


Fig. 3. 2D volume slice of SECT and DECT volumes: 80 kV (A), 190 kV (B), fused dual energy scans with weighting factors of 0.3 (C), 0.5 (D), and 0.7 (E). Numbering of phases: 1 = Air trapped in voids and cracks, 2 = graphite, 3 = combined quartz and clay, 4 = muscovite, 5 = HFO after muscovite, 6 = HFO vein-fill, and 7 = hematite. The yellow (F) and red (G) boxes, respectively, show a section of a graphite flake (centre of image) and N-S extending cracks and a small hematite crystal (lower centre). The graphite flake appears sharper, and the cracks are less blurred in the fused DECT scan with a weighting factor 0.5 (G). Note the small flake in the lower right of the slice, which is barely visible in the SECT volume slices compared to the DECT scan, and the reduced beam hardening introduced by a small hematite crystal. Window levelling was set to Smart Contrast for each slice to maximize contrast between each phase.

occasionally bended or broken apart along basal cleavage (Fig. 2A–C). Some large clusters contain minor intergrowth of HFO. Quartz is present as primary subhedral (up to $600~\mu m$ in length) (Fig. 2A) or small recrystallized crystals ($50-250~\mu m$ in lengths) showing triple junction texture (Fig. 2C). Muscovite occurs as euhedral to subhedral crystals ($500~\mu m-6~m m$ in length) showing different degrees of alteration with HFO occasionally occurs along the basal cleavage planes (Fig. 2A). HFO are also present as veinlet and cracks infills as well as along grain boundaries (Fig. 2A, and Fig. 2C). Moreover, it may appear pseudomorph after muscovite and hematite (Fig. 2A). The ore is interspersed with cracks and features numerous cavities (Fig. 2B).

3.2. Evaluation of CT image quality

3.2.1. Qualitative analysis

The volume slices depicted in Fig. 3 represent SECT scans conducted at different energy levels: a LV scan (80 kV), an HV scan (190 kV), and their corresponding fused DECT volume slices, generated using varying weighting factors of 0.3, 0.5, and 0.7. Seven different grey value intensities can be identified in both the SECT volume slices and DECT slices. These correspond to (see numbers from 1 to 7 in Fig. 3A):

- 1) air in voids and cracks (from dark grey to black),
- 2) graphite (dark grey),
- 3) combined quartz and clay (grey),

- 4) muscovite (from grey to light grey),
- 5) HFO after muscovite (light grey),
- 6) HFO vein-fill (from light grey to whitish), and
- 7) hematite (white).

The SECT and DECT volume slices exhibit notable differences in noise, contrast, and sharpness. The SECT images generally appear noisier compared to the DECT images (Fig. 3A–B). Among the DECT images, the one with a weighting factor of 0.7 exhibits the highest noise level (Fig. 3E). On the other hand, the images with weighting factors of 0.3 and 0.5 show similar noise, with the latter being slightly less noisy (Fig. 3C–D).

Considering contrast, the SECT volume slice obtained at 190 kV and the DECT with a weighting factor of 0.7 show lower contrast than the other images. The other volume slices have similar contrast, with the data set reconstructed with a weighting factor of 0.3 appearing to have less contrast.

Regarding image sharpness, the SECT images exhibit partial blurring and occasionally show double edges (see yellow box in Fig. 3A and Fig. 3F). These issues are alleviated in all the DECT images, with the one at 0.5 weighting factor appearing the sharpest among them (see red box in Fig. 3D and Fig. 3G).

The histogram in Fig. 4 displays the grey value distribution of the 80 kV scan (Fig. 4A), the 190 kV scan (Fig. 4B), and the corresponding fused DECT data sets with a weighting factor of 0.5 (Fig. 4C). Each peak

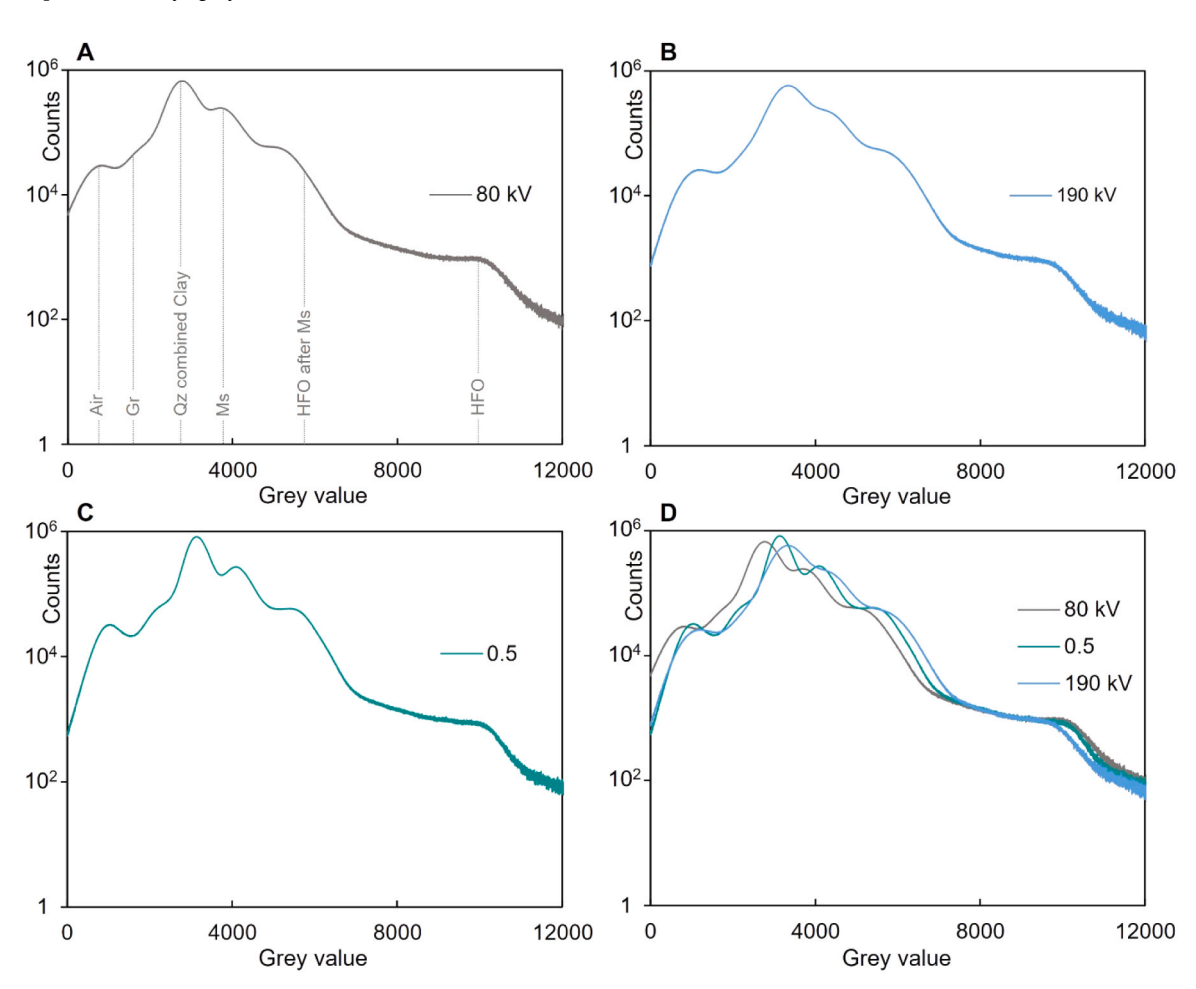


Fig. 4. Histogram of grey value distribution (range from 0 to 12000) of SECT scans – 80 kV (A) and 190 kV (B) – and the corresponding fused 80 kV x 190 kV x 0.5 dataset (C). A peak in the histogram indicates a phase contained in the scanned object. A) Histogram of the 80 kV scan showing the mean grey values of the phases comprising the samples apart from hematite which is out of the histogram range. Note that air refers to the air trapped within voids and cracks. D) Grey value distribution of 80 kV, 190 kV, and the 80 kV x 190 kV x 0.5 DECT, note the evolved shoulder indicating graphite in the fused DECT dataset. Abbreviations:Gr = graphite, Qtz = quartz, Ms = muscovite, HFO = hydrated iron(III) oxide-hydroxides.

Table 2

Mean CNR values and results of Fisher LSD test for each material area and parameter combination from 10 ROIs for each phase and structure. Group A is the highest (marked dark green), and Group J is the lowest (marked dark orange) CNR group. Members of the same group have no significant differences. The mean CNR values which belong only to the best or only to the worst group of the considered material area, are marked in bold. The highest mean CNR value in each material area is marked bright green, and the lowest is bright orange. All mean CNR values belonging to the best group are highlighted in green, those belonging to the worst in orange.

				Material are	ea						
Parameter combination	M1: 0	Graphite - Quartz & Clay		M2: Graphite - Air	M3: Mu	ıscovite - HFO	M4: M	M4: Muscovite - Quartz & Clay			
	mean CNR	t-Test groups	mean CNR	t-Test groups	mean CNR	t-Test groups	mean CNR	t-Test groups			
60 kV	4.331	GH	2.863	J	5.012		G 3.800	H I			
80 kV	4.518	F G	3.307	I J	5.726	DEF	G 4.681	E F G			
170 kV	3.554	1	3.985	н	5.745	DEF	G 3.488	1			
180 kV	3.658	H	4.402	DEFGH	5.417	F	G 3.460	1			
190 kV	3.548	1	4.213	F G H	5.578	E F	G 3.329	1			
60 kV x 170 kV x 0.3	4.840	CDEFG	4.000	н	6.142	BCDEF	4.555	E F G			
60 kV x 170 kV x 0.5	5.329	C D E	4.992	C D	6.812 A	B C D	5.788	C D			
60 kV x 170 kV x 0.7	6.167	A B	5.697	AB	6.924 A	ВС	6.334	ВС			
60 kV x 180 kV x 0.3	5.034	CDEFG	4.029	н	5.996	CDEF	G 4.572	E F G			
60 kV x 180 kV x 0.5	5.079	CDEFG	4.674	CDEFG	6.287	BCDEF	5.182	D E			
60 kV x 180 kV x 0.7	4.610	E F G	4.800	CDEF	6.123	BCDEF	4.360	F G H			
60 kV x 190 kV x 0.3	5.304	CDEF	4.103	GH	6.358	BCDEF	4.917	E F			
60 kV x 190 kV x 0.5	5.505	ВС	5.083	ВС	6.973 A	ВС	4.930	E F			
60 kV x 190 kV x 0.7	5.462	B C D	5.027	C D	6.687 A	B C D	4.542	E F G			
80 kV x 170 kV x 0.3	4.637	E F G	3.779	H I	6.315	BCDEF	4.337	F G H			
80 kV x 170 kV x 0.5	4.707	DEFG	4.224	F G H	6.590 A	B C D E	4.480	F G			
80 kV x 170 kV x 0.7	4.426	G	4.318	E F G H	6.435	BCDEF	4.238	G H			
80 kV x 180 kV x 0.3	4.655	E F G	4.124	GH	6.585 A	B C D E	4.328	F G H			
80 kV x 180 kV x 0.5	6.401	A	6.062	A	7.646 A	N.	7.056	A			
80 kV x 180 kV x 0.7	4.734	DEFG	5.006	C D	6.615 A	BCDE	4.461	F G H			
80 kV x 190 kV x 0.3	6.417	Α	4.906	C D E	7.131 A	В	6.595	A B			
80 kV x 190 kV x 0.5	6.594	A	5.711	A	7.216 A	В	6.701	A B			
80 kV x 190 kV x 0.7	4.640	E F G	4.873	C D E	6.590 A	B C D E	4.275	F G H			

The mean CNR values for the SECT data within the ROIs range from 2.863 (MA2) to 5.745 (MA3), and global CNR values – from 2.80 to 5.66 (Table 2). In contrast, mean CNR values for the DECT data range from 3.779 (MA2) to 7.646 (MA3), and global CNR values – from 3.73 to 7.44. Notably, in every ROI, most of the CNR values of the DECT datasets consistently surpass those of the SECT datasets regardless of the weighting factor. Except for MA3, most CNR values of the fused DECT datasets differ significantly from those of the SECT scans.

in the histogram corresponds to specific phases within the scanned sample. The better defined the peaks are, the less overlapping grey values exist, indicating a more definite phase assignment. The distinctness of the peaks and the degree of overlapping grey values differ significantly between the SECT and DECT histograms (Fig. 4D). The grey value material areas of materials like cavities and quartz are more compressed in the DECT histogram, indicating a more improved image contrast and a reduced overlap of grey values. Furthermore, the DECT histogram reveals an additional shoulder (Fig. 4C–D) that corresponds to graphite which is not visible in the other histograms (Fig. 4A–B).

3.2.2. Quantitative analysis

The quantitative analysis is based on the detailed CNR analysis of the established ROIs. Four different material areas (MA1, MA2, MA3, and MA4) were defined (see Section 2.5), and the analysis was individually performed for each material area. The mean CNR values obtained for ten ROIs from all SECT and DECT volumes are shown in Table 2 and Table A. 2 (Appendix).

The DECT combination $80~kV \times 180~kV \times 0.5$ shows the highest mean and global CNR values for the MA2, MA3, and MA4. These combinations always belong to group A. In MA1, the combination $80~kV \times 190~kV \times 0.5$ exhibits the highest global and mean CNR value. In all ROIs, the mean CNR values of these two settings are significantly different compared to the vast majority of the DECT combinations. The $80~kV \times 180~kV \times 0.5$ is in the same significance group (group A) as $80~kV \times 190~kV \times 0.5$ (all material areas), $60~kV \times 170~kV \times 0.7$ (MA1, MA2, and MA3), $80~kV \times 190~kV \times 0.5$ is in the same significance group (group A) as $80~kV \times 190~kV \times 0.5$ (all material areas), $60~kV \times 170~kV \times 0.7$ (all material areas), $80~kV \times 190~kV \times 0.5$ (all material areas), $80~kV \times 170~kV \times 0.5$ (all material areas), $80~kV \times 170~kV \times 0.5$ (MA1, MA3, and MA4). In contrast, the $80~kV \times 170~kV$ DECTs exhibit statistically lowest CNR values compared to the other DECT combinations.

The weighting factor 0.5 exhibits, in most cases, the highest absolute

CNR values and is significantly better for some DECT combinations than other weighting factors on the MA1, MA2, and MA4. In contrast, apart from the 80~kV~x~190~kV DECT combination, factor 0.3 often shows significantly lower CNR values. Especially on MA2, datasets calculated with the weighting factor 0.3 are significantly worse compared to the factors 0.5 and 0.7 of all DECT combinations apart from 80~kV~x~170~kV (same significance among all weighting factors). In MA3, there is no statistical difference compared to the fused datasets of the same combination and different weighting factors.

Regarding the CNR values of the SECT datasets, 80 kV shows the highest global and mean CNR values than 60 kV SECT (Table 2). In MA4, this difference is statistically significant. Furthermore, the HV datasets exhibit the lowest CNR values in MA1 and MA4. In contrast, concerning MA2, the CNR calculations of the LV datasets show significantly worse values than the HV datasets. Within MA3, no general trend can be determined.

4. Discussion

DECT has primarily been utilized in geoscientific research for material decomposition, extracting density, and effective atomic number $(Z_{\rm eff})$ information on the basis of the raw projection data to differentiate minerals in rocks and ores [38–41]. However, the quantification of improved image quality using DECT has not been elaborately discussed. Addressing this research gap, a comprehensive evaluation of image quality enhancement using DECT on a polyphase graphite ore was conducted by analysing the contrast-to-noise ratio (CNR) and Q factors of SECT and fused DECT scans. SECT scans were acquired at different tube energies and combined with varying weighting factors, further allowing to explore the impact of different proportions of the fused energy spectra on image quality.

4.1. DECT data acquisition

The findings revealed that fused DECT datasets have a positive and statistically significant effect on image quality in terms of CNR and Q factors regardless of the weighting factor applied compared to the SECT scans. Two mechanisms account for the improved contrast.

First, mathematically, the improved CNR and Q factors exhibited by DECT compared to SECT is attributed to the determined standard deviations of the reconstructed DECT data (denominator in both formulas). During CT data acquisition, the detector captures the materialdependent attenuation of X-ray radiation from the exposed sample, converting it into different photon intensity that are then converted into CT numbers and stored in the form of projection data. The linear combination of SECT datasets in DECT involves mathematically merging the pixel values of corresponding projection pictures from each dataset. Through fusion, the projection data is averaged based on the weighting factor, leading to higher information density. Consequently, outliers become less significant, resulting in a lower standard deviation in the DECT data. This reduction in standard deviation contributes to the enhanced CNR and Q factors observed in DECT compared to SECT. This is a purely statistical effect, however, and a similar degree of noise reduction might be expected from combining two SECT datasets acquired at the same energy.

Second, the specimens' materials constituents (e.g., graphite, quartz, hematite, HFO, air) exhibit a different attenuation behaviour at different X-ray energies. At lower X-ray energies, the photoelectric effect dominates, which is more sensitive to the material's atomic number (Z) (proportional to Z⁴⁻⁵) [48,49]. This effect is particularly effective for phases with higher Z values. On the other hand, at higher X-ray energies, Compton scattering becomes more prevalent, and the attenuation is more dependent on the material's electron density [48]. For low-absorbing phases and those comprising similar densities (e.g., graphite, quartz), lower X-ray energies are better to avoid underexposure, as the photoelectric effect provides better contrast in these cases. Conversely, higher X-ray energies should be applied for high-absorbing phases (e.g., hematite, HFO), typically with higher Z values, to ensure sufficient penetration of the material and avoid overexposure. With DECT, two X-ray spectra are acquired at different energy levels. These energy-specific datasets contain complementary information about the attenuation characteristics of the scanned materials. Combining these datasets through DECT leverages the advantages of both lower and higher X-ray energies, resulting in improved contrast and more accurate differentiation of materials with a broad range of attenuation behaviours. The varying contrasts observed in the SECT and DECT datasets directly result from the different absorption properties of the minerals present in the sample at different X-ray energies. When comparing the LV scans and DECT combinations with equal energy fractions (weighting factor 0.5), it was generally noted that datasets acquired at 60 kV provide slightly worse CNR values compared to combinations at 80 kV, although not always significantly. Considering the target material is tungsten, the efficiency of producing characteristic X-rays decreases notably at energies below 80 kV. As a result, Bremsstrahlung becomes a greater proportion of the X-ray spectrum and the average energy of the X-ray beam decreases [50]. This, in turn, results in a higher degree of attenuation of lower energy X-rays and introduces noise. These effects may be amplified through the polymineralic nature of the sample. An exception is the 80 kV x 170 kV DECT combination, whose CNR (and Q factor) values belong to the same significance group as the 60 kV SECT combinations. However, this combination is the one with the most negligible difference in the fused energy spectra. According to [43], an appropriate distance between the energy of the X-ray spectra of the two measurements is essential for obtaining proper DECT data. The results of the CNR (and Q factor) values of the 80 kV x 170 kV, independent from the weighting factor and ROI, indicate that this difference was too small, thus underlining this finding.

DECT combinations utilizing higher LV x HV energies consistently

demonstrate significantly higher CNR (and Q factor) values with a weighting factor of 0.5 compared to the other DECT reconstructions. This observation is likely influenced by the specific mineralogy and microstructure of the sample, which tends to require higher X-ray energy levels from both spectra. This may also explain why the $60\,kV$ x $170\,kV$ combination, with a weighting factor of 0.7, exhibits significantly higher CNR values than the same combination of 0.3 and 0.5. Otherwise, 21/24 of the fused reconstructed datasets exhibit the highest CNR values compared to weighting factors 0.3 and 0.7.

4.1.1. Grey value distribution in the evaluated material areas

Notably, all HV SECT settings exhibited statistically higher CNR values for MA2 compared to those obtained with the LV spectra. The underlying reason for this disparity lies again in the energy-dependent components of Compton scattering and photoelectric absorption of Xrays. Generally, scans at lower energies tend to provide better contrast due to the photoelectric effect, which is highly sensitive to the atomic number (Z) and particularly effective for phases with high Z [42,51]. However, graphite (Z = 6) and the main gases of air (nitrogen (Z = 7)and oxygen (Z = 8)) have very similar Z. On the other hand, there exists sufficient difference in their densities (graphite = 2.1 g/cm³, air = 1.2e-3 g/cm³ at 20 °C). This density discrepancy becomes the dominant factor influencing X-ray attenuation at higher voltages, where the Compton effect prevails. As a result, scans with higher voltages demonstrate improved contrasts between graphite and air, as the Compton effect is more sensitive to the density of a material, compensating for the minor atomic number difference between graphite, and the major constituents of air. This is also reflected in the fused DECT datasets, where the weighting factor of 0.7 provided higher CNR values for three of the six combinations. Thus, the results show that the significant changes in the contrasts of the DECT datasets depend on both the combined voltages and the weighting factor.

A comparable trend is observed regarding the global CNR values of the various DECT combinations (Table 2). However, it is noteworthy that the CNR values within MA3 do not exhibit as significant differences as those observed in other material areas (e.g., MA2, MA1). Statistically, this can be attributed to the partly substantial variation in mean attenuation and standard deviation of the individual regions of interest (ROIs) within the HFO. From a mineralogical perspective, this could be influenced by varying Fe contents or different stadiums of pseudomorphism of HFO after muscovite at the locations where the ROIs were placed. This interpretation is supported by the varying brightness levels observed in the grey-scale images (Fig. 3), which suggest heterogeneity in the mineral composition within MA3. These compositional variations in the HFO may account for the observed similarity in CNR (and Q factor) values across different DECT combinations within this specific material area.

4.2. Limitations and future studies

The recommendations regarding the energy spectra and the weighting factor for the DECT fusion to be applied are based on one specific sample. Although the sample was extensively evaluated with 18 parameter combinations that were based on the establishment of 1840 grey value analysis, more empirical data on these types of geomaterials needs to be collected to further validate the findings. Additionally, like SECT, DECT also faces limitations in distinguishing between phases with rather similar or identical attenuation properties such as quartz and clay. This constraint is inherent to all CT techniques and impacts on DECT as well [37]. Also, mineralogical data is necessary prior to any DECT analysis so that CT scans can be interpreted correctly [20,22,52]. Time is a further limiting factor when it comes to DECT, as it requires acquiring two SECT scans to generate the DECT datasets. This process at least doubles time and costs compared to obtaining SECT data alone. The contrast variations observed in the DECT datasets indicate that the combination of different X-ray energies significantly affects the image

quality. However, to further evaluate the mechanism contributing to the superior image quality, future studies should compare DECT scans with SECT scans having double the acquisition time. Regarding the preferential choice of the image quality metrics used, it was observed that CNRs are more responsive to noise in the background material. At the same time, Q factors are less susceptible to the same noise within a material area (Table A.2). This behaviour could be attributed to the denominator in the Q factor calculation, which considers the noise of both ROIs in the material area. Regardless, as the scope of this study did not encompass an in-depth comparison of these metrics, further research is needed to validate this observation. Lastly, future studies could consider the effect of other scanning parameters (e.g., exposure time and current) on the image quality of the fused DECT data.

The variation in contrast values observed in this study emphasise the critical role of selecting the appropriate X-ray energy level to optimise image quality and contrast, particularly in the context of heterogeneous geomaterials like the ones studied here. One of the central challenges in CT scanning, however, is finding the optimal scan settings for a given material due to the polychromatic nature of the X-ray beam. A common approach is calculating the linear attenuation coefficient for each phase in the sample [21,26]. However, a polychromatic X-ray source is used in most CT applications, and the linear attenuation coefficient's energy dependency must be considered. Simulation software can be an effective tool for determining these optimal settings, especially in cases where the material's composition and internal structure are known in advance (e. g., workpieces) [24,53]. However, the situation becomes more complex when dealing with geological materials. Buyse et al. successfully calculated reconstructed attenuation coefficients to differentiate between minerals in a heterogeneous geological sample for a given CT setup using simulation software [52]. The simulations assumed a monomineralic sample while considering factors such as sample geometry, chemical composition, and size. In practice, the ability to identify the appropriate scanning conditions for geological samples through simulation remains challenging due to the uncertainty surrounding the spatial arrangement and grain size distribution of the phases within the sample. Regardless, DECT proves to be significantly superior to SECT in terms of achieving high-quality data, making it particularly valuable for less experienced operators seeking to enhance image quality and data accuracy.

4.3. Implications for mineral characterisation

The accurate extraction of quantitative mineralogical data from ores and their constituents, such as volume, shape, grain size, and distribution, relies on the segmentation of CT datasets after volume reconstruction to isolate and classify the phases of interest. CT images are commonly segmented based on their grayscale intensities [42]. More advanced machine learning segmentation techniques also utilize object shape and pixel texture for feature classification [42,54,55]. High image-quality CT datasets are essential for precise quantitative analysis, particularly for heterogeneous ores with a broad range of X-ray attenuation among their constituents, which may also exhibit similar grayscale intensities. To enhance image quality, datasets are often processed after reconstruction using various filtering methods. However, filtering techniques usually present a trade-off: filters that decrease noise also blur the image (e.g. median filter, gaussian filter, and averaging filter), while those that increase image sharpness introduce noise into the image, leading to a potential data loss [56,57]. In contrast, DECT effectively improves the image quality without compromising data quality. This advantage makes DECT particularly beneficial for more accurate segmentation, resulting in more precise and reliable identification of mineral phases and features. The enhanced image quality

achieved for the investigated ore with the DECT-based approach provides a robust foundation for subsequent segmentation processes, ultimately enhancing the accuracy and reliability of quantitative mineralogical analysis.

The object studied in this research is a graphite ore. Previous studies have demonstrated the added value of CT for characterising graphite ores and enhancing resource efficiency [22,58]. Building upon these findings, the present study offers additional insights into acquiring high-quality data on graphite ores. DECT, capable of addressing varying attenuation demands, shows great potential for the characterisation of such ores, which typically consist of high-absorbing materials like pyrite and hematite, along with air, while graphite exhibits low attenuation. By effectively managing these different attenuation properties, DECT enables the acquisition of appropriate contrasts for each phase, thereby enhancing the analysis of graphite ores and contributing to more accurate and detailed assessments of graphite ores.

5. Conclusion

This study explored the use of DECT for enhancing grayscale contrast of a heterogenous polyphase graphitic ore. A sequential fusion approach was applied to combine data obtained from different X-ray energy scans at high spatial resolution. Various X-ray energy spectra were combined with varying weighting factors to determine the favourable contribution of each energy level applied, thereby aiming to provide the best possible attenuation of each phase.

The results reveal that DECT provides complementary information on the material's attenuation characteristics that significantly improves the image grayscale contrast between individual phases comprising the investigated specimen compared to SECT. Considering the specimen investigated, higher energy DECT combinations and the weighting factor of 0.5 tend to provide the best image contrast regarding CNR and Q factor. In addition, the fusion method applied also enhances image sharpness.

Given the complex microstructure and mineralogical composition of ores and the fact that the results are based on one particular sample, more research is needed to validate the findings of this study on a wider range of ore samples. Nevertheless, the findings suggest that DECT can be a valuable tool for improving 3D characterisation of polyphase graphitic ores. The additional grayscale contrast and image sharpness provided by DECT may allow for more accurate segmentation and thus quantitative mineralogical analysis. This could help to improve the understanding of graphite deposits and the development of more efficient extraction processes.

Declaration of Competing Interest

The authors declare that they have no known competing financial interests or personal relationships that could have appeared to influence the work reported in this paper.

Acknowledgements

The authors would like to thank Alper Bakic from ProCon X-ray GmbH for his work on the Python script. Two anonymous referees are greatly acknowledged for their constructive criticism of the manuscript

Appendix

Table A.1

Mean Q factor values and results of Fisher LSD test for each material area and parameter combination from 10 ROIs for each phase and structure. Group A is the highest (marked dark green), and Group G is the lowest (marked dark orange) Q factor group. Members of the same group have no significant differences. The mean Q factor values, which belong only to the best or only to the worst group of the focused material area, are marked in bold. The highest mean Q factor value in each material area is marked bright green, and the lowest is bright orange. All mean Q factor value members of the best group drew green, of the worst – orange.

	Material area																												
Parameter combination	M1: Graphite - Quartz & Clay							M2: Graphite - Air						M3: Muscovite - HFO							M4: Muscovite - Quartz & Cla				Clay				
	mean Q	mean Q t-Test groups				mean Q t-Test groups							mean Q t-Test groups								mean Q t-Test gro			oup	s				
60 kV	2.990					F	G	Н	1.928						ŀ	Н	3.776							Н	2.709				F G
80 kV	3.076				Е	F	G		2.237						ŀ	н	4.294				Е	F	G	Н	3.240		D	Е	
170 kV	2.404							1	2.825				Е	F	G		4.294				Е	F	G	н	2.450				G
180 kV	2.508							ΗI	2.951			D	Е	F	G		4.068						G	Н	2.418				G
190 kV	2.359							- 1	2.924				Е	F	G		4.153					F	G	н	2.305				G
60 kV x 170 kV x 0.3	3.941	A B	С						2.747					F	G		4.672			CI	E	F	G		3.227		D	Е	
60 kV x 170 kV x 0.5	3.968	A B	С						3.447		В						5.182	Α	В	CI	0				4.056	C			
60 kV x 170 kV x 0.7	4.077	A B							3.915	Α							5.263	Α	В	CI	0				4.351	ВС			
60 kV x 180 kV x 0.3	3.437		С	D	Е	F	G		2.717						G		4.547			- 1) E	F	G		3.251		D	Е	
60 kV x 180 kV x 0.5	3.465		С	D	Е	F	G		3.079		C	D	Е	F			4.786		В	CI	E	F	G		3.383		D	Е	
60 kV x 180 kV x 0.7	3.176			D	Е	F	G		3.159		ВС	D	Ε				4.623			CI	E	F	G		3.058		D	Е	F
60 kV x 190 kV x 0.3	3.616	В	С	D	Е				2.792					F	G		4.896	Α	В	CI	E	F			3.448		D		
60 kV x 190 kV x 0.5	3.649	АВ	С	D					3.377		ВС						5.304	Α	В	CI	0				3.448		D		
60 kV x 190 kV x 0.7	3.488		С	D	Е	F			3.378		ВС						5.147	Α	В	CI	0				3.134		D	Е	F
80 kV x 170 kV x 0.3	3.078				Е	F	G		2.630						G		4.798		В	CI) E	F	G		3.061		D	Е	F
80 kV x 170 kV x 0.5	3.098			D	Е	F	G		2.957			D	Е	F	G		5.006	Α	В	CI	E				3.154		D	Е	F
80 kV x 170 kV x 0.7	2.910						G	ΗI	3.070		C	D	Е	F			4.849		В	CI	E	F			2.982			Е	F
80 kV x 180 kV x 0.3	3.195			D	Е	F	G		2.866				Е	F	G		4.925	Α	В	CI	E				3.088		D	Е	F
80 kV x 180 kV x 0.5	4.232	Α							3.855	Α							5.675	Α							4.824	A			
80 kV x 180 kV x 0.7	3.190			D	Е	F	G		3.318		ВС						4.930	Α	В	CI) E	F			3.110		D	Е	F
80 kV x 190 kV x 0.3	4.087	A B							3.308		ВС						5.356	Α	В	С					4.526	A B			
80 kV x 190 kV x 0.5	3.860	А В	С						3.874	Α							5.495	Α	В						4.546	A B			
80 kV x 190 kV x 0.7	3.067				Е	F	G		3.294		ВС	D					4.973	Α	В	CI	E				2.950			Е	F

10mography of materials and Structures 4 (2024) 100021

Table A. 2Global, mean, and standard deviation values of the CNR and Q-factor measurements of each material area.

	Materia	ıl area																									
Parameter combination	M1: Gra	M1: Graphite - Quartz & Clay						M2: Graphite - Air						M3: Muscovite - HFO							M4: Muscovite - Quartz & Clay						
	CNR	CNR			Q-factor			CNR			Q-factor			CNR			r		CNR			Q-factor					
	global	mean	std	global	mean	std	global	mean	std	global	mean	std	global	mean	std	global	mean	std	global	mean	std	global	mean	std			
60 kV	4.24	4.33	0.53	2.93	2.99	0.31	2.80	2.86	0.52	1.90	1.93	0.28	5.01	5.01	0.96	3.77	3.78	0.76	3.67	3.80	0.45	2.64	2.71	0.29			
80 kV	4.42	4.52	0.55	3.00	3.08	0.39	3.07	3.31	0.38	2.21	2.24	0.23	5.66	5.73	0.91	4.28	4.29	0.67	4.40	4.68	0.89	3.07	3.24	0.58			
170 kV	3.52	3.55	0.41	2.39	2.40	0.25	3.93	3.99	0.57	2.81	2.82	0.28	5.63	5.75	1.21	4.25	4.29	0.85	3.46	3.49	0.26	2.44	2.45	0.14			
180 kV	3.62	3.66	0.32	2.49	2.51	0.17	4.77	4.40	0.48	2.93	2.95	0.28	5.38	5.42	0.94	4.07	4.07	0.68	3.45	3.46	0.20	2.42	2.42	0.17			
190 kV	3.46	3.55	0.54	2.34	2.36	0.23	4.17	4.21	0.41	2.92	2.92	0.23	5.54	5.58	0.89	4.14	4.15	0.66	3.30	3.33	0.25	2.29	2.31	0.17			
60 kV x 170 kV x 0.3	4.81	4.84	0.58	3.35	3.94	1.76	3.88	4.00	0.68	2.70	2.75	0.34	6.08	6.14	1.17	4.66	4.67	0.89	4.42	4.56	0.51	3.15	3.23	0.32			
60 kV x 170 kV x 0.5	5.76	5.33	0.66	3.82	3.97	0.50	4.79	4.99	0.88	3.37	3.45	0.46	6.69	6.81	1.31	5.15	5.18	0.93	5.53	5.79	0.90	3.90	4.06	0.59			
60 kV x 170 kV x 0.7	6.00	6.17	0.83	3.95	4.08	0.66	5.43	5.70	1.19	3.80	3.92	0.63	6.78	6.92	1.30	5.23	5.26	0.88	5.97	6.33	1.18	4.15	4.35	0.73			
60 kV x 180 kV x 0.3	4.93	5.03	0.57	3.38	3.44	0.32	3.90	4.03	0.95	2.67	2.72	0.56	5.91	6.00	1.23	4.52	4.55	0.93	4.46	4.57	0.47	3.19	3.25	0.29			
60 kV x 180 kV x 0.5	5.01	5.08	0.48	3.40	3.47	0.33	4.58	4.67	0.83	3.05	3.08	0.47	6.17	6.29	1.35	4.76	4.79	0.98	5.13	5.18	1.53	3.64	3.38	1.09			
60 kV x 180 kV x 0.7	4.57	4.61	0.37	3.15	3.18	0.25	4.76	4.80	0.60	3.14	3.16	0.37	6.01	6.12	1.29	4.60	4.62	0.89	4.33	4.36	0.39	3.04	3.06	0.26			
60 kV x 190 kV x 0.3	5.22	5.30	0.48	3.56	3.62	0.30	4.03	4.10	0.58	2.77	2.79	0.34	6.31	6.36	1.27	4.88	4.90	0.96	4.83	4.92	0.43	3.40	3.45	0.25			
60 kV x 190 kV x 0.5	5.44	5.51	0.52	3.60	3.65	0.33	5.05	5.08	0.43	3.36	3.38	0.28	6.83	6.97	1.22	5.28	5.30	0.80	4.88	4.93	0.37	3.42	3.45	0.23			
60 kV x 190 kV x 0.7	5.20	5.46	1.36	3.45	3.49	0.34	4.95	5.03	0.55	3.35	3.38	0.25	6.57	6.69	1.39	5.11	5.15	0.93	4.52	4.54	0.23	3.12	3.13	0.19			
80 kV x 170 kV x 0.3	4.59	4.64	0.32	3.01	3.08	0.33	3.73	3.78	0.42	2.62	2.63	0.19	6.19	6.32	1.13	4.76	4.80	0.82	4.24	4.34	0.48	3.00	3.06	0.32			
80 kV x 170 kV x 0.5	4.67	4.71	0.34	3.04	3.10	0.31	4.15	4.22	0.66	2.94	2.96	0.24	6.44	6.59	1.24	4.96	5.01	0.88	4.40	4.48	0.44	3.11	3.15	0.27			
80 kV x 170 kV x 0.7	4.39	4.43	0.38	2.87	2.91	0.27	4.23	4.32	0.69	3.06	3.07	0.27	6.29	6.44	1.27	4.80	4.85	0.87	4.18	4.24	0.35	2.96	2.98	0.20			
80 kV x 180 kV x 0.3	4.59	4.66	0.48	3.11	3.20	0.43	4.09	4.12	0.42	2.84	2.87	0.29	6.37	6.59	1.38	4.88	4.93	0.86	4.26	4.33	0.32	3.05	3.09	0.18			
80 kV x 180 kV x 0.5	6.21	6.40	1.01	4.00	4.23	0.78	5.73	6.06	1.43	3.68	3.86	0.79	7.44	7.65	1.67	5.64	5.68	0.99	6.61	7.06	1.33	4.62	4.82	0.76			
80 kV x 180 kV x 0.7	4.70	4.73	0.31	3.17	3.19	0.24	4.93	5.01	0.58	3.26	3.32	0.40	6.54	6.62	1.28	4.93	4.93	0.85	4.43	4.46	0.26	3.10	3.11	0.20			
80 kV x 190 kV x 0.3	5.95	6.42	2.12	3.84	4.09	1.16	4.79	4.91	0.79	3.24	3.31	0.43	6.89	7.13	1.47	5.32	5.36	0.96	6.07	6.60	1.45	4.23	4.53	0.90			
80 kV x 190 kV x 0.5	6.29	6.59	1.20	4.10	3.86	1.50	5.60	5.71	0.78	3.80	3.87	0.52	6.99	7.22	1.45	5.44	5.50	0.89	6.26	6.70	1.31	4.30	4.55	0.80			
80 kV x 190 kV x 0.7	4.58	4.64	0.56	3.05	3.07	0.22	4.84	4.87	0.40	3.28	3.29	0.15	6.44	6.59	1.20	4.94	4.97	0.77	4.23	4.27	0.28	2.93	2.95	0.17			

References

- D.N. Sutherland, P. Gottlieb, Application of automated quantitative mineralogy in mineral processing, Miner. Eng. 4 (1991) 753–762, https://doi.org/10.1016/0892-6875(91)90063-2.
- [2] S.J.B. Reed, Electron Microprobe Analysis and Scanning Electron Microscopy in Geology, Cambridge University Press,, 2005.
- [3] Y. Liu, Z. Hu, M. Li, S. Gao, Applications of LA-ICP-MS in the elemental analyses of geological samples, Chin. Sci. Bull. 58 (32) (2013) 3863–3878, https://doi.org/ 10.1007/s11434-013-5901-4.
- [4] B. Lavina, P. Dera, R.T. Downs, Modern x-ray diffraction methods in mineralogy and meosciences, Rev. Mineral. Geochem. 78 (1) (2014) 1–31, https://doi.org/ 10.2138/rmg.2014.78.1.
- [5] L.Y. Le Bras, R. Bolhar, L. Bam, B.M. Guy, G.M. Bybee, P.A.M. Nex, Three-dimensional textural investigation of sulfide mineralisation from the Loolekop carbonatite-phoscorite polyphase intrusion in the Phalaborwa Igneous Complex (South Africa), with implications for ore-forming processes, MinMag 85 (4) (2021) 514-531, https://doi.org/10.1180/mgm.2021.32.
- [6] F. Reyes, J.J. Lin, S.J. Neethling, Quantifying mineral liberation by particle grade and surface exposure using x-ray microCT, Miner. Eng. 125 (2018) 75–82, https://doi.org/10.1016/j.mineng.2018.05.028.
- [7] S.G. Le Roux, A. Du Plessis, A. Rozendaal, The quantitative analysis of tungsten ore using X-ray microCT: case study, Comput. Geosci. 85 (1) (2015) 75–80, https:// doi.org/10.1016/j.cageo.2015.09.009.
- [8] B. Godel, High-resolution x-ray computed tomography and its application to ore deposits: from data acquisition to quantitative three-dimensional measurements with case studies from Ni-Cu-PGE deposits, Econ. Geol. 108 (8) (2013) 2005–2019, https://doi.org/10.2113/econgeo.108.8.2005.
- [9] J.R. Kyle, A.S. Mote, R.A. Ketcham, High resolution X-ray computed tomography studies of Grasberg porphyry Cu-Au ores, Papua, Indonesia, Min. Depos. 43 (5) (2008) 519–532, https://doi.org/10.1007/s00126-008-0180-8.
- [10] D.A. Jerram, M.D. Higgins, 3D analysis of rock textures: quantifying igneous microstructures, Elements 3 (4) (2007) 239–245, https://doi.org/10.2113/ gselements.3.4.239.
- [11] F. Mees, R. Swennen, M. van Geet, P. Jacobs, Applications of X-ray computed tomography in the geosciences, Geol. Soc. Publ. House (2003).
- [12] S. Lohmeier, R.R. Gainov, A. Hodgkin, Morphological characterization of lode gold in the auriferous quartz veins at MPopo mine, Angola, by computed tomography and optical microscopy, Appl. Earth Sci. 132 (2) (2023) 65–89, https://doi.org/ 10.1080/25726838.2023.2219116.
- [13] V. Cnudde, M.N. Boone, High-resolution X-ray computed tomography in geosciences: a review of the current technology and applications, Earth-Sci. Rev. 123 (4) (2013) 1–17, https://doi.org/10.1016/j.earscirev.2013.04.003.
- [14] S. Spencer, D. Sutherland, Stereological correction of mineral liberation grade distributions estimated by single sectioning of particles, Image Anal. Stereol. 19 (3) (2000) 175–182, https://doi.org/10.5566/ias.v19.p175-182.
- [15] T. Ueda, T. Oki, S. Koyanaka, Experimental analysis of mineral liberation and stereological bias based on X-ray computed tomography and artificial binary particles, Adv. Powder Technol. 29 (23) (2018) 462–470, https://doi.org/ 10.1016/j.apt.2017.11.004.
- [16] T. Ueda, T. Oki, S. Koyanaka, Stereological bias for spherical particles with various particle compositions, Adv. Powder Technol. 27 (4) (2016) 1828–1838, https:// doi.org/10.1016/j.apt.2016.06.016.
- [17] P.J. Withers, C. Bouman, S. Carmignato, V. Cnudde, D. Grimaldi, C.K. Hagen, E. Maire, M. Manley, A. Plessis, S.R. Stock, X-ray computed tomography, Nat. Rev. Methods Prim. 1 (2021), 18, https://doi.org/10.1038/s43586-021-00015-4.
- [18] S. Carmignato, W. Dewulf, R. Leach, Industrial X-Ray Computed Tomography, Springer International Publishing, Cham, 2018.
- [19] H. Villarraga-Gómez, E.L. Herazo, S.T. Smith, X-ray computed tomography: from medical imaging to dimensional metrology, Precis. Eng. 60 (2) (2019) 544–569, https://doi.org/10.1016/j.precisioneng.2019.06.007.
- [20] P.I. Guntoro, Y. Ghorbani, P.-H. Koch, J. Rosenkranz, X-ray microcomputed tomography (μCT) for mineral characterization: a review of data analysis methods 9 (2019) 183, https://doi.org/10.3390/min9030183.
- [21] F. Reyes, Q. Lin, O. Udoudo, P.D. Lee, S.J. Neethling, Calibrated X-ray micro-tomography for mineral ore quantification, Miner. Eng. 110 (2017) 122–130, https://doi.org/10.1016/j.mineng.2017.04.015.
- [22] L.T. Krebbers, B.G. Lottermoser, X. Liu, Computed tomography of flake graphite ore: data acquisition and image processing, Minerals 13 (2) (2023) 247, https://doi.org/10.3390/min13020247.
- [23] A. Jansson, L. Pejryd, A dual-energy approach for improvement of the measurement consistency in computed tomography, Meas. Sci. Technol. 27 (11) (2016), 115013, https://doi.org/10.1088/0957-0233/27/11/115013.
- [24] N. Grozmani, D. Chupina, B. Montavon, R.H. Schmitt, Sinogram interpretability based CT artefact reduction for multi-material workpieces, Nondestruct. Test. Eval. 37 (5) (2022) 679–691, https://doi.org/10.1080/10589759.2022.2091134.
- [25] L.C. Bam, J.A. Miller, M. Becker, I.J. Basson, X-ray computed tomography: practical evaluation of beam hardening in iron ore samples, Miner. Eng. 131 (2018) 206–215, https://doi.org/10.1016/j.mineng.2018.11.010.

- [26] J.R. Kyle, R.A. Ketcham, Application of high resolution X-ray computed tomography to mineral deposit origin, evaluation, and processing, Ore Geol. Rev. 65 (B2) (2015) 821–839, https://doi.org/10.1016/j.oregeorev.2014.09.034.
- [27] L.C. Bam, J.A. Miller, M. Becker, A mineral x-ray linear attenuation coefficient tool (MXLAC) to assess mineralogical differentiation for x-ray computed tomography scanning, Minerals 10 (2020) 441, https://doi.org/10.3390/min10050441.
- [28] M. Voigt, J.A. Miller, A.N. Mainza, L.C. Bam, M. Becker, The robustness of the gray level co-occurrence matrices and x-ray computed tomography method for the quantification of 3D mineral texture, Minerals 10 (2020) 334, https://doi.org/ 10.3390/min10040334.
- [29] R. Garnett, A comprehensive review of dual-energy and multi-spectral computed tomography, Clin. Imaging 67 (2020) 160–169, https://doi.org/10.1016/j. clinimae 2020 07 030
- [30] L. Martin, A. Tuysuzoglu, W.C. Karl, P. Ishwar, Learning-based object identification and segmentation using dual-energy CT images for security, IEEE Trans. Image Process. 24 (11) (2015), https://doi.org/10.1109/TIP.2015.2456507.
- [31] C. Bauer, R. Wagner, J. Leisner, Detection of foreign items in laundry industry—a dual energy XRT approach, Eng. Proc. 21 (1) (2022) 14, https://doi.org/10.3390/ engproc2022021014.
- [32] J. Leisner, C. Bauer, R. Wagner, Circular Economy: Material Sorting in Waste Streams Using Dual Energy X-ray Transmission (2022).
- [33] S. Chen, X. Zhong, S. Dorn, N. Ravikumar, Q. Tao, X. Huang, M. Lell, M. Kachelriess, A. Maier, Improving generalization capability of multiorgan segmentation models using dual-energy CT, IEEE Trans. Radiat. Plasma Med. Sci. 6 (1) (2022) 79–86, https://doi.org/10.1109/TRPMS.2021.3055199.
- [34] J.G. Fletcher, N. Takahashi, R. Hartman, L. Guimaraes, J.E. Huprich, D.M. Hough, L. Yu, C.H. McCollough, Dual-energy and dual-source CT: Is there a role in the abdomen and pelvis? Radiol. Clin. North Am. 47 (1) (2009) 41–57, https://doi. org/10.1016/j.rcl.2008.10.003.
- [35] H. Scheffel, P. Stolzmann, T. Frauenfelder, T. Schertler, L. Desbiolles, S. Leschka, B. Marincek, H. Alkadhi, Dual-energy contrast-enhanced computed tomography for the detection of urinary stone disease, Invest. Radiol. 42 (12) (2007) 823–829, https://doi.org/10.1097/RLI.0b013e3181379bac.
- [36] F.F. Behrendt, B. Schmidt, C. Plumhans, S. Keil, S.G. Woodruff, D. Ackermann, G. Mühlenbruch, T. Flohr, R.W. Günther, A.H. Mahnken, Image fusion in dual energy computed tomography, Invest. Radiol. 44 (1) (2009), https://doi.org/10.1097/RLI.0b013e31818c3d4b.
- [37] Fornaro, Dual- and multi-energy CT: approach to functional imaging, Insights Imaging 2 (2011), https://doi.org/10.1007/s13244-010-0057-0.
- [38] M. Martini, P. Francus, L. Di Schiavi Trotta, P. Després, Identification of common minerals using stoichiometric calibration method for dual-energy CT, Geochem Geophys Geosyst 22 (11) (2021) 225, https://doi.org/10.1029/2021GC009885.
- [39] Yousef Ghorbani, Megan Becker, Jochen Petersen, Sameer H. Morar, Aubrey Mainza, J.-P. Franzidis, Use of X-ray computed tomography to investigate crack distribution and mineral dissemination in sphalerite ore particles, Miner. Eng. 24 (12) (2011) 1249–1257, https://doi.org/10.1016/j.mineng.2011.04.008.
- [40] H. Alves, I. Lima, J.T. de Assis, A.A. Neves, R.T. Lopes, Mineralogy evaluation and segmentation using dual-energy microtomography, X-Ray Spectrom. 44 (3) (2015) 99–104, https://doi.org/10.1002/xrs.2582.
- [41] H. Alves, I. Lima, R.T. Lopes, Methodology for attainment of density and effective atomic number through dual energy technique using microtomographic images, Appl. Radiat. Isot. 89 (2014) 6–12, https://doi.org/10.1016/j. apradisp. 2014.01.018
- [42] S.R. Stock, MicroComputed Tomography: Methodology and Applications, CRC Press, Boca Raton, FL 33487–2742, 2019.
- [43] B. Schmidt, T. Flohr, Principles and applications of dual source CT, Phys. Med. 79 (2020) 36–46, https://doi.org/10.1016/j.ejmp.2020.10.014.
- [44] Volume Graphics GmbH, VGSTUDIO MAX 3.5.0, Heidelberg, Germany, 2021.
- [45] A. Kraemer, E. Kovacheva, G. Lanza, Projection based evaluation of CT image quality in dimensional metrology, eJNDT 20 (8) (2015).
- [46] A. Du Plessis, M. Tshibalanganda, S.G. Le Roux, Not all scans are equal: X-ray tomography image quality evaluation, Mater. Today Commun. 22 (2020), 100792, https://doi.org/10.1016/j.mtcomm.2019.100792.
- [47] M. Reiter, D. Weiß, C. Gusenbauer, M. Erler, C. Kuhn, S. Kasperl, J. Kastner, Evaluation of a histogram-based image quality measure for X-ray computed tomography, eJNDT 19 (6) (2014).
- [48] A.A. Markowicz, X.-ray Physics: In: Handbook of X-ray Spectrometry, Marcel Dekker, Inc., New York, 1993.
- [49] R. van Grieken, A. Markowicz, Handbook of X-Ray Spectrometry, CRC Press,, 2001.
- [50] J.A. Seibert, X-ray imaging physics for nuclear medicine technologists. Part 1: basic principles of X-ray production, J. Nucl. Med. Technol. 32 (3) (2004) 139–147.
- [51] J. Hsieh, Computed Tomography: Principles, Design, Artifacts, and Recent Advances, SPIE Press,, 2003.
- [52] F. Buyse, S. Dewaele, M.N. Boone, V. Cnudde, Combining automated mineralogy with x-ray computed tomography for internal characterization of ore samples at the microscopic scale, Nat. Resour. Res 32 (2) (2023) 461–478, https://doi.org/ 10.1007/s11053-023-10161-z.
- [53] R.H. Schmitt, A. Buratti, N. Grozmani, C. Voigtmann, M. Peterek, Model-based optimisation of CT imaging parameters for dimensional measurements on multimaterial workpieces, CIRP Ann. 67 (1) (2018) 527–530.

- [54] X. Li, G. Zhang, K. Li, W. Zheng, Deep Learning and Its Parallelization, in: R. Buyya, R.N. Calheiros, A.(E.)V. Dastjerdi (Eds.), Big Data: Principles and Paradigms, Elsevier/Morgan Kaufmann, Cambridge, MA, USA, 2016, pp. 95–118.
- [55] S. Chauhan, Phase Segmentation and Analysis of Tomographic Rock Images Using Machine Learning Techniques. Doctoral dissertation, Universitäts-und Landesbibliothek Darmstadt, 2019.
- [56] V. Kovalevsky, Modern Algorithms for Image Processing, Apress,, Berkeley, CA, 2019.
- [57] R.C. Gonzalez, R.E. Woods, Digital Image Processing, 4th ed., Pearson, 330 Hudson Street, New York, NY 10013, 2017.
- [58] Y. Ren, J. Li, X. Sun, Z. Li, Z. Sun, Genesis of metal sulfides and its significance on graphite mineralization in the Huangyangshan graphite deposit, East Junggar, Xinjiang Province, China, Minerals 12 (11) (2022) 1450, https://doi.org/10.3390/ min12111450.